Monthly Notices
of the
ROYAL ASTRONOMICAL SOCIETY

MNRAS **537,** 2586–2601 (2025)
Advance Access publication 2025 February 5

https://doi.org/10.1093/mnras/staf183

Multiband flux and spectral variability study of the flaring activity in BL Lacertae during its 2020 outburst

Aditi Agarwal ,[1]★ V. Agrawal,[2] S. Zola ,[3] Swarnendu Jana,[1] M. S. Bisht,[4] A. Raj,[4,5] V. Kouprianov ,[6] Daniel E. Reichart,[6] D. B. Caton[7] and James W. Dawidson[8]

[1] *Center for Cosmology and Science Popularization (CCSP), SGT University, Budhera, Delhi-NCR 122006, India*
[2] *Embibe, Diamond District, Old Airport Road, Bengaluru 560008, India*
[3] *Astronomical Observatory, Jagiellonian University, ul. Orla 171, 30244 Krakow, Poland*
[4] *Indian Centre for Space Physics, 466 Barakhola, Netai Nagar, Kolkata 700099, West Bengal, India*
[5] *Uttar Pradesh State Institute of Forensic Science (UPSIFS), Aurawan, PO Banthra, Lucknow226401 (UP), India*
[6] *Department of Physics and Astronomy, University of North Carolina at Chapel Hill, Chapel Hill, NC 27599, USA*
[7] *Dark Sky Observatory, Department of Physics and Astronomy, Appalachian State University, Boone, NC 28608, USA*
[8] *Department of Astronomy, University of Virginia, 530 McCormick Rd, Charlottesville, VA 22904, USA*

Accepted 2025 January 28. Received 2025 January 28; in original form 2024 April 11

ABSTRACT

In this work, we present the results of recent quasi-simultaneous multiband optical observations (in *BVRI*) of the blazar BL Lacertae over diverse time-scales. For this study, the source was observed from 2020 September–October using six different telescopes around the world, collecting ∼5800 photometric image frames in *BVRI*. The source displays many episodes of significant intraday variability, and the amplitude increases with the brightness of the target. Moreover, the object also showed significant variability on a short-term basis, with flux variability amplitudes of 85.6 per cent, 78.9 per cent, 93.4 per cent, and 67.6 per cent in *B*, *V*, *R*, and *I* passbands, respectively. The colour–magnitude analysis of the source displays dominantly bluer-when-brighter behaviour on both intraday and short time-scales, which can be attributed to the energetic processes in the jet. Correlation analysis points towards a strong correlation between optical bands with no firmly detectable time lags. Moreover, we also performed a periodicity search using the Lomb–Scargle and weighted wavelet *Z*-transform methods and found plausible indications of the presence of quasi-periodicity in the blazar. We also generated spectral energy distributions for nights with quasi-simultaneous observations in all four bands and found the spectral index to range from 2.9–3.2, which can be ascribed to a strong jet contribution. We discuss the results within the framework of prospective source intrinsic and extrinsic scenarios.

Key words: galaxies: active – BL Lacertae objects: general – BL Lacertae objects: individual: BL Lacertae.

1 INTRODUCTION

Blazars are a rare subclass of active galactic nuclei (AGNs) in which the highly collimated relativistic jets are nearly aligned along our line of sight within $\leq 15^\circ$ (Urry & Padovani 1995). Blazars consist of two classes, namely BL Lacertae objects (BL Lacs) and flat-spectrum radio quasars (FSRQs). BL Lacs have featureless optical spectra or very weak emission lines with equivalent width (EW) ≤ 5 Å, whereas FSRQs show strong broad emission lines in their composite optical/UV spectra (Ghisellini et al. 1997). Moreover, various studies have found that FSRQs have radiatively efficient optically thick and geometrically thin accretion discs, unlike BL Lacs, which have been found to have a radiatively inefficient accretion disc (Ghisellini & Celotti 2001; Ghisellini 2019; Agarwal 2023, and references therein).

Blazars display rapid flux, spectral, and polarization variability at all frequencies and on diverse time-scales ranging from minutes to even years. Based on the variability time-scales, flux variability can be divided into microvariability or intraday variability (IDV) for variations occurring on time-scales of a few minutes to less than a day (Wagner & Witzel 1995), short-term variability (STV) for changes taking place on day to month time-scales (Gopal-Krishna et al. 2003), and long-term variability (LTV) for variations of months to years (Bhatta 2021). During the past few decades, there have been numerous campaigns dedicated to blazar variability, with a focus on IDV in various frequency bands (Heidt & Wagner 1996; Montagni et al. 2006; Poon, Fan & Fu 2009; Bhatta & Webb 2018; Weaver et al. 2020; Agarwal et al. 2021, 2022, and references therein). However, the exact cause of variability in blazars is still very much debated today.

The broad-band spectral energy distributions (SEDs, e.g. Fossati et al. 1997) of blazars in the $\log \nu F_\nu$ versus $\log \nu$ plot display a double-peaked spectrum. The lower energy hump peaking in optical/ultraviolet (UV) or even X-rays is well understood as coming from Doppler-boosted synchrotron emission by relativistic electrons in the magnetized plasma of the jet, while the high-energy hump extending from X-rays to γ-rays is likely due to inverse Compton (IC) processes, where the seed photons are either the synchrotron photons

---

★ E-mail: aditiagarwal.phy@gmail.com

from the jet itself (synchrotron self-Compton, SSC: Ghisellini & Maraschi 1989; Maraschi, Ghisellini & Celotti 1992) or external to jets, such as photons originating from the broad-line region (BLR), torus, and accretion disc (AD), and the process in this case is known as external Compton (EC: Begelman & Sikora 1987; Sikora, Begelman & Rees 1994). Apparently low-luminosity sources, such as BL Lacs, have very weak or no contamination from an AD, BLR, or torus, and therefore the high-energy emission can most likely be attributed to SSC. Apart from the above processes, the detection of high-energy neutrinos in blazars indicates the association of high-energy components with proton–synchrotron or proton–photon processes, broadly known as hybrid models (Böttcher et al. 2013; Ansoldi et al. 2018, and references therein). Blazars are classified further according to the position of their synchrotron peak frequency ($\nu_{\rm syn}$) as high synchrotron peaked blazars (HSPs) with $\nu_{\rm syn} \geq 10^{15}$ Hz, intermediate frequency synchrotron peaked (ISP) with $10^{14} < \nu_{\rm syn} < 10^{15}$ Hz, or low synchrotron frequency peaked (LSP) with $\nu_{\rm syn} \leq 10^{14}$ Hz (Abdo et al. 2010; Ackermann et al. 2011). Some BL Lacs have also shown extreme behaviour, with synchrotron peak frequency $\geq 10^{17}$, and are popularly classified as extremely high synchrotron peaked BL Lacs (EHBLs: Foffano et al. 2019).

BL Lacertae, located at a redshift of 0.069 (Vermeulen et al. 1995), is the archetype of BL Lacs and is classified as either a low-frequency peaked BL Lac (LBL) or intermediate-frequency peaked (IBL), as its synchrotron peak has been found to shift in different scenarios (Hervet, Boisson & Sol 2016; Nilsson et al. 2018, and references therein). BL Lacertae has been identified as a TeV blazar (Neshpor et al. 2001) and also has been reported with strong and rapid flux variations in different energy bands over time-scales ranging from minutes to even years (Hagen-Thorn et al. 2002; Villata et al. 2002, 2004a; Raiteri et al. 2013; Meng et al. 2017; Agarwal et al. 2023, and references therein), thus making it a target of numerous coordinated multi-wavelength campaigns (Marscher et al. 2008; Raiteri et al. 2009; Sasada et al. 2020; Weaver et al. 2020; Sahakyan & Giommi 2022). The majority of observations of BL Lacertae have found the source to display flux and polarization variability on diverse time-scales (Gaur et al. 2015; Weaver et al. 2020; Agarwal et al. 2023). Many studies have detected microvariations in the target, followed by spectral flattening with an increase in the source brightness (Papadakis, Villata & Raiteri 2007; Bhatta & Webb 2018). As pointed out by Papadakis et al. (2003), the perturbations of different emitting regions in the Doppler-boosted jet could be responsible for such microvariations. Such perturbations can lead to the injection of relativistic particles on time-scales shorter than the average sampling of the light curve.

The source has recently undergone historic high flux activity during 2020–2021 in optical to γ-ray wavelengths (Blanch 2020a,b; Cheung 2020; Grishina & Larionov 2020; Jankowsky & Wagner 2020; Ojha & Valverd 2020; Steineke et al. 2020; Kunkel et al. 2021; Marchini et al. 2021; Jorstad et al. 2022, and references therein). During this unprecedented activity phase, BL Lacertae reached its brightest state ever observed, with an R-band magnitude of 11.271 ± 0.003 mag on 2021 July 30 (Kunkel et al. 2021).

BL Lacertae has been extensively explored for the presence of quasi-periodicities (QPOs) on diverse time-scales, and several such instances have been reported at various frequencies: for example, Hagen-Thorn et al. (2002) proposed a periodicity of 308 days in the 22-yr series of photometric and polarimetric optical observations of BL Lacertae, a periodicity of ~ 8 yr was reported by Villata et al. (2004b) during the radio outburst and was later also claimed by Villata et al. (2009), and a 680-day periodicity was found by Sandrinelli et al. (2017) in the R-band and gamma-ray observations. The physics behind such year-long periodicities can be extremely complicated. The above works suggested various processes, including the presence of a binary supermassive black hole (SMBH), a helically moving plasma blob, or precession of the relativistic jet. Recently, Jorstad et al. (2022) studied the source during its pre-outburst state in 2020, where they found a quasi-periodicity of $\sim$13 h in optical and gamma-ray frequencies. They also detected a strong correlation between both frequencies with no temporal lag, thus indicating that the same emission mechanism is at play for both optical and gamma-rays. The authors have suggested that kink instabilities in the relativistic jet might explain the correlation between optical and gamma-ray light curves. The temporal growth of the kink instability also led to the detection of a QPO within a period of a few days.

In this work, we have studied the temporal and spectral behaviour of BL Lacertae in optical bands during an exceptional flaring period. We also searched for multi-frequency time lags on intranight to short time-scales, along with the presence or absence of periodicity during the observation period. The work is organized as follows: Section 2 provides a brief overview of the various telescopes and data reduction procedures used. Section 3 describes various analysis techniques used in the work, while the results are presented in Section 4. Finally, a discussion of the findings and conclusions are presented in Section 5.

2 OBSERVATIONS, DATA ANALYSIS, AND DATA REDUCTION

The photometric observations of the target BL Lacertae were obtained in B, V, R, and I bands using six ground-based telescopes. The source was observed from 2020 September–October over 16 observation nights and gathering $\sim$ 5800 $BVRI$ frames. The six different telescopes used are as follows: 50-cm Corrected Dall–Kirkham Astrograph (OAUJ-CDK500, telescope A) of the Astronomical Observatory operated by the Jagiellonian University, Krakow, Poland; 60-cm Rapid Response Robotic Telescope (RRRT, telescope B) of the Fan Mountain Observatory; Kirkham astrograph telescope (KRK, telescope C) of the Jagiellonian University, Krakow, Poland; 40-cm telescope of the Montana Learning Center (MLC-COS16, telescope D); 40-cm telescope of the Dark Sky Observatory (DSO, telescope E); and 40-cm PROMPT-USASK telescope of Sleaford Observatory (PSASK, Telescope C). The technical details of the above telescopes are given in table 1 of Agarwal et al. (2023). The log of observations used here is presented in Table 1. Telescopes A, B, D, E, and F are operated in robotic mode by the Skynet Robotic Telescope Network software (Zola et al. 2021).

For data reduction, we used the standard IRAF[1] cleaning tasks, which include bias/dark subtraction, flat-fielding, and cosmic-ray removal. Cleaning of raw images was followed by extraction of instrumental magnitudes by concentric circular aperture photometry using the Dominion Astronomical Observatory Photometry (DAOPHOT II) software (Stetson 1987, 1992). Every night, we observed more than three local standard stars in the same field (Ghisellini et al. 1997; Villata et al. 1998). To perform differential photometry, a pair of non-varying standard stars (stars B and C) are selected with magnitude and colour comparable with the source and also in close proximity to the blazar. Since the source and the standard stars are taken from the same field of view, we get highly reliable magnitude values under the

---

[1] IRAF is distributed by the National Optical Astronomy Observatories, which are operated by the Association of Universities for Research in Astronomy, Inc., under a cooperative agreement with the National Science Foundation.

Table 1. Log of photometric observations for BL Lacertae. The columns are (1) date of observations, (2) telescope used, (3) number of data points in each filter on a particular night. Columns 4, 5, and 6, are same as columns 1, 2, and 3, respectively.

Date of observations (yyyy mm dd)	Telescope	Number of data points				Date of observations (yyyy mm dd)	Telescope	Number of data points			
		B	*V*	*R*	*I*			*B*	*V*	*R*	*I*
2020 09 15	A	17	192	16	192	2020 09 25	F	0	0	6	0
2020 09 15	C	14	15	109	13	2020 09 27	A	39	39	310	40
2020 09 16	B	0	0	41	0	2020 09 27	D	0	0	6	0
2020 09 17	A	12	199	12	176	2020 09 30	B	18	18	18	0
2020 09 17	D	0	0	2	0	2020 10 04	B	12	13	14	0
2020 09 18	C	0	6	448	6	2020 10 04	C	10	10	649	10
2020 09 19	A	6	54	58	5	2020 10 04	E	0	0	42	0
2020 09 19	B	0	0	38	0	2020 10 05	A	0	0	36	0
2020 09 19	D	0	0	4	0	2020 10 05	C	9	10	199	9
2020 09 20	A	0	131	128	3	2020 10 05	E	0	0	70	0
2020 09 20	B	0	0	18	0	2020 10 06	A	74	0	0	0
2020 09 21	B	0	0	6	0	2020 10 06	B	15	16	16	0
2020 09 21	C	16	16	815	0	2020 10 06	C	0	0	391	0
2020 09 22	B	0	0	40	0	2020 10 06	E	0	0	105	0
2020 09 22	C	184	189	184	187	2020 10 07	F	0	0	3	0
2020 09 24	B	0	0	6	0						

same weather, air mass, and measurement conditions. The calibrated light curves (LCs) of BL Lacertae indicated a few data points with large errors. To mitigate any discrepancy during the analysis of the blazar LCs, we removed those data points that had errors more than ten times the median of errors in the LC. A more detailed description of the data reduction process followed here can be found in Agarwal et al. (2021).

3 ANALYSIS METHODOLOGY

3.1 Variability study

Quantifying flux variability of the source on intraday time-scales helps us delineate the properties of the emission region and the dominant radiation mechanisms. To study the variability properties of BL Lacertae on intraday time-scales, we used only those LCs that spanned at least 1 hour of observations. Following this criterion, we have 53 light curves over 23 observation nights, of which 13 observation nights have multiband data sets while the remaining 10 are single-wavelength only. The time range of the LCs differs substantially, ranging from 2–10 hours and with very different sampling. Also, for dates with more than one intranight LC obtained from two different telescopes, there was a large window with no data points between the two intranight LCs. Therefore, we analysed both data sets as two separate LCs.

To quantify variability in these light curves, we have employed the most common and robust statistical tests, namely, C, F, and χ^2 tests, which are discussed briefly below.

3.1.1 *C test*

The variability detection criterion, C test, described in Romero, Cellone & Combi (1999) is defined as

$$C_1 = \frac{\sigma(\mathrm{BL} - \mathrm{S_B})}{\sigma(\mathrm{S_B} - \mathrm{S_C})}, \quad C_2 = \frac{\sigma(\mathrm{BL} - \mathrm{S_C})}{\sigma(\mathrm{S_B} - \mathrm{S_C})}, \tag{1}$$

where BL$-$S$_\mathrm{B}$, BL$-$S$_\mathrm{C}$, and S$_\mathrm{B}$–S$_\mathrm{C}$ are the differential instrumental LCs of the blazar (BL) against the standard star B (S$_\mathrm{B}$), BL against the standard star C (S$_\mathrm{C}$), and S$_\mathrm{B}$ against S$_\mathrm{C}$, respectively, while σ(BL$-$S$_\mathrm{B}$), σ(BL$-$S$_\mathrm{C}$), and σ(S$_\mathrm{B}$–S$_\mathrm{C}$) are the standard deviations of the respective LCs. A C value is calculated by taking a mean over C_1 and C_2. Where $C \geq 2.576$, significant variability is said to be detected at a confidence level of 99.5 per cent or above; otherwise the light curve is marked non-variable. Zibecchi et al. (2017) studied IDV in AGNs using different statistical methods and found that the C test gave highly reliable results.

3.1.2 *F test*

The F test (Zibecchi et al. 2017) compares the differential variances of the source with the differential variances of the standard stars. The statistic is defined as

$$F_1 = \frac{\sigma^2(\mathrm{BL} - \mathrm{S_B})}{\sigma^2(\mathrm{S_B} - \mathrm{S_C})}, \quad F_2 = \frac{\sigma^2(\mathrm{BL} - \mathrm{S_C})}{\sigma^2(\mathrm{S_B} - \mathrm{S_C})}, \tag{2}$$

where BL$-$S$_\mathrm{B}$, BL$-$S$_\mathrm{C}$, and S$_\mathrm{B}$–S$_\mathrm{C}$ are the differential instrumental magnitudes of the blazar against the star B, blazar against star C, and star B against star C, respectively, while σ^2(BL–S$_\mathrm{B}$), σ^2(BL–S$_\mathrm{C}$), and σ^2(S$_\mathrm{B}$–S$_\mathrm{C}$) are the variances of the respective LCs. Taking the average of F_1 and F_2 gives the mean F value, which is then compared with the critical value, $F_\mathrm{c} = F^{(\alpha)}_{\nu_\mathrm{BL},\nu_\mathrm{S}}$, where ν_BL and ν_S are the number of degrees of freedom for the blazar and standard stars, respectively, calculated as the number of measurements, N, minus 1 ($\nu = N - 1$). The significance level, α, is set as 0.1 per cent and 1 per cent (i.e. 3σ and 2.576σ) for this work. The LC is considered to be variable if the F value is more than the critical value and the null hypothesis (i.e. no variability) is rejected.

3.1.3 χ^2 *test*

Further, we also used the χ^2 test to check for the presence/absence of variability, which is interpreted as

$$\chi^2 = \sum_{i=1}^{N} \frac{(V_i - \overline{V})^2}{e_i^2}, \tag{3}$$

where $\overline{V}$ is the mean magnitude and V_i the magnitude corresponding to the ith observation, with corresponding uncertainty e_i. The IRAF package does not give exact values of uncertainties, and the values of theoretical uncertainties have been estimated to be smaller by 1.3–1.75 (Gopal-Krishna et al. 2003). For the data used here, the factor has been found to be ~ 1.6, and thus we multiplied the errors obtained from data reduction by this factor. When the χ^2 value is greater than the critical χ^2 value, $\chi^2_{\alpha,\nu}$ (α is the significance level and $\nu = N - 1$ is the degree of freedom), it indicates the presence of significant variability.

According to Zibecchi et al. (2017, 2020), the F test tends to give false positives, while the C criterion tends to give false negatives. F and C tests estimate the target's variability relative to standard stars, whereas the χ^2 test estimates the variability relative to the estimated uncertainties, as shown above. Therefore, all the variability tests learn about different aspects of the data, which motivates us to combine the results of multiple methods and get a unanimous vote. We consider the target variable only if all three tests result in 3σ significance.

3.1.4 Percentage amplitude variation

To estimate the absolute range of variability in our LCs, we used variability amplitude parameter A, which is defined as (Heidt & Wagner 1996)

$$A = 100 \times \sqrt{(m_{\max} - m_{\min})^2 - 2\langle e^2 \rangle}\ [\%], \tag{4}$$

where $m_{\max}$ and $m_{\min}$ are the maximum and minimum calibrated magnitudes of the blazar and $\langle e^2 \rangle$ the mean squared error of the measurements.

3.1.5 Spectral variability

Variations in the optical flux of blazars are frequently correlated with their spectral variations. In order to study the spectral variability of BL Lacertae on intraday and short time-scales, we built colour–magnitude diagrams (CMDs) of $B-V$, $B-I$, $V-R$, and $R-I$ colour changes with respect to the R-band magnitude. For that, the calibrated magnitudes were first dereddened for Galactic extinction using the values from the National Aeronautics and Space Administration (NASA)/Infrared Processing and Analysis Center (IPAC) Extragalactic Database: $A_B = 0.43$ mag, $A_V = 0.54$ mag, $A_R = 0.64$ mag, and $A_I = 0.80$ mag.

The CMDs were built using quasi-simultaneous data points in the above frequency pairs. To determine quantitatively the relation between the colour index (CI) and the brightness of the source in the R band (R), CMDs were fitted by a straight line $CI = mR + C$ and the values for the slope, m, and the constant, c, along with the null hypothesis probability (p) and correlation coefficient (r), are derived for these fits. The null hypothesis is that the variations are assumed not to be chromatic.

A positive slope here indicates that the spectra tend to be steeper as the target brightens, also popularly known as the bluer-when-brighter (BWB) trend. Meanwhile, a negative slope between two quantities signifies a redder-when-brighter (RWB) trend. A particular CMD with a large p value indicates the probability of correlations being caused by random noise. Therefore, to consider a CMD significant at 99 per cent confidence level, we require the null hypothesis probability p to be ≤ 0.01.

3.1.6 Cross-correlation analysis

Multiband light curves present an opportunity to investigate a correlation between two frequencies and estimate possible time lags among them. To check for a correlation between light curves of different bands and identify possible time delays, we employed the discrete correlation function (DCF) and the z-transformed DCF (ZDCF).

The DCF was introduced by Edelson & Krolik (1988) and is one of the best statistical tools used to quantify the correlation between two unevenly sampled data sets. To calculate the DCF between two discrete data sets, we first calculate a set of unbinned DCFs (UDCFs). As described by Edelson & Krolik (1988), these UDCF values are binned using a suitable time lag, and the mean DCF of M pairs is expressed as

$$DCF(\tau) = \frac{1}{M} UDCF_{ij}, \tag{5}$$

where M is the number of pairs with time lag values lying in the τ interval. Errors in each DCF bin are calculated as

$$\sigma_{\mathrm{DCF}(\tau)} = \frac{\sqrt{\sum_{k=1}^{M} (UDCF_k - DCF(\tau))^2}}{M - 1}. \tag{6}$$

The ZDCF is a more advanced and improved technique for estimating the correlation and time lag between the LCs of different bands. The ZDCF uses equal population binning and Fisher's z-transform on the DCF to correct for biases of the DCF method. Furthermore, the ZDCF follows a form of adaptive binning, which ensures a high statistical significance of each bin by using various bin width values. More details on the ZDCF can be found in Alexander (2013). We have used publicly available codes[2] of the methodology given by Alexander (1997). The error is calculated in z-space using equation (7) of Alexander (2013) and transformed back to r-space using equation (8) in that work. A more detailed description of the error calculation can be found in Alexander (2013).

3.2 Periodicity search

Periodicity in blazars has been actively pursued, and a few instances with a time-scale of a few years have been reported (Bhatta et al. 2016b). Periodicity searches in time series can help us disentangle mysteries related to the structure of the central engine. In order to search for periodicity in the intraday and short-term LCs of the source, BL Lacertae, we used two widely accepted techniques, namely the Lomb–Scargle periodogram (LSP: Lomb 1976; Scargle 1982) and weighted wavelet Z-transform (WWZ: Foster 1996). Both of these methods have a strong edge in handling the challenge of unevenly spaced data and are well-suited for picking up sinusoidal signals even in irregular data sets.

3.2.1 Lomb–Scargle periodogram

The LSP technique was first proposed by Lomb (1976), later extended by Scargle (1982), and has been generalized further for more practical purposes by Press & Rybicki (1989). The LSP is an improved version of the conventional discrete Fourier periodogram (DFP), which minimizes the least-squares fitting of the sine waves. Therefore, compared with the DFP, the LSP is less affected by uneven sampling of the data set. We generated LSPs for our data using the following

---

[2] https://www.weizmann.ac.il/particle/tal/research-activities/software

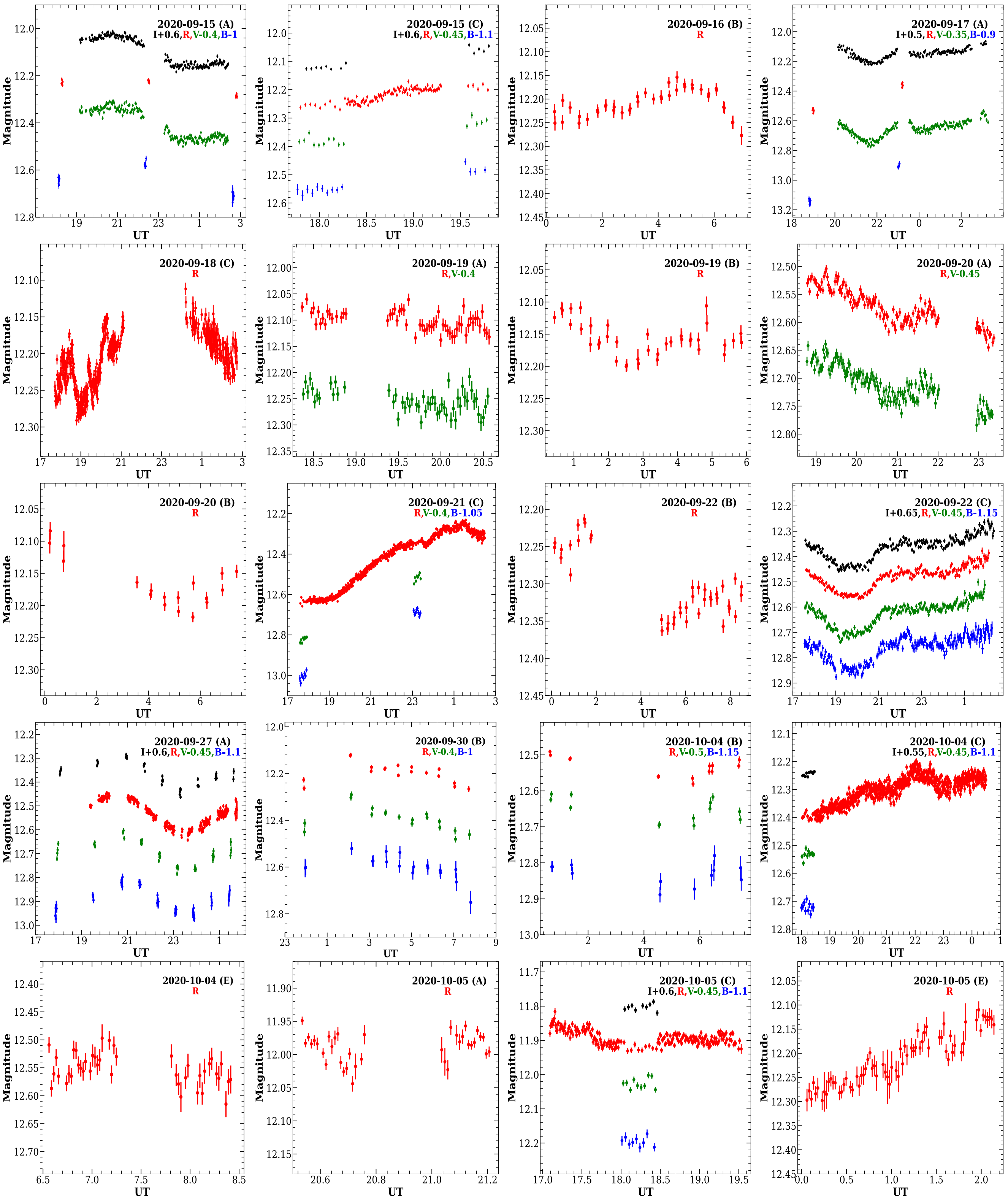

Figure 1. Nightly optical light curves of BL Lacertae in *B*, *V*, *R*, and *I* passbands. The observation date and telescope used are shown in each plot.

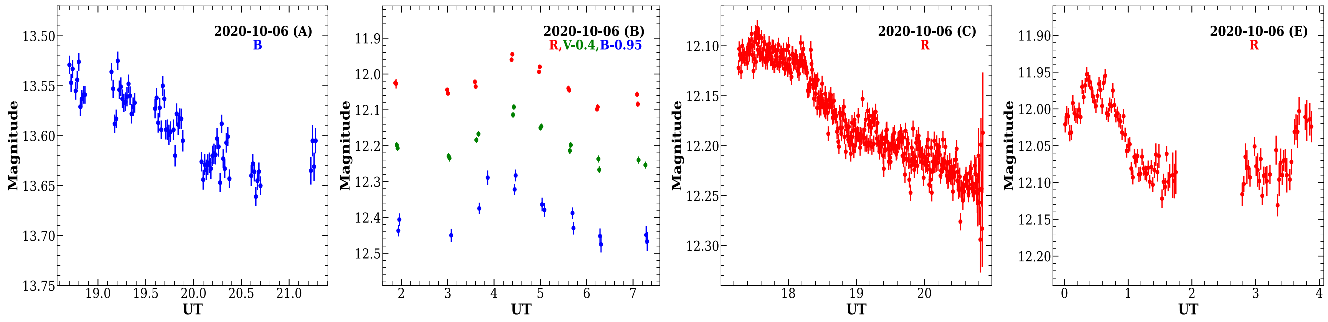

Figure 1. *Continued.*

equation:

$$P_{\rm LS}(f)=\frac{1}{2}\left\{\frac{\left(\sum_n g_n\cos(2\pi f[t_n-\tau])\right)^2}{\sum_n\cos^2(2\pi f[t_n-\tau])}+\frac{\left(\sum_n g_n\sin(2\pi f[t_n-\tau])\right)^2}{\sum_n\sin^2(2\pi f[t_n-\tau])}\right\}, \quad (7)$$

where τ is specified for each f to ensure time-shift invariance. It needs to be noted that the generalized LSP (GLSP),[3] which accounts for measurement errors in the analysis, has also been employed in a number of works for periodicity searches. Similar periods were identified when we used the GLSP approach to evaluate the light curves in addition to the LSP method.

3.2.2 *Weighted wavelet Z-transform*

Periodic or quasi-periodic signals may or may not be persistent throughout the observation period. The LSP approach does not account for time variations in the periodic signal information. Quasi-periodic oscillations in actual astronomical systems can grow and change in amplitude and frequency over time. The weighted WWZ approach, which is widely used in the study of blazar sources, has been shown to be a more helpful tool in these situations. WWZ has the added advantage of decomposing the signal in the time and frequency domains, thus allowing us to assess the persistence of periodicity in certain time series data. This method is a more complex method than the widely used discrete wavelet transform (DFT) for detecting periodicities in unevenly spaced light curves. Even with regularly spaced data, the DFT can produce statistical behaviour that is not trivial. We refer to Foster (1996) for a thorough description of this and the WWZ approach.

The weighted projection of the data vector onto the subspace made up of three trial functions is the foundation of the WWZ approach:

$$\begin{cases}\phi_1(t)=1(t),\\ \phi_2(t)=\cos(\omega(t-\tau)),\\ \phi_3(t)=\sin(\omega(t-\tau)),\end{cases} \quad (8)$$

when an n-dimensional vector represents each trial function,

$$\boldsymbol{\phi_i(t)}=[\phi_i(t_1),\phi_i(t_2),...,\phi_i(t_n)], \quad (9)$$

where $i = 1, 2, 3$.

It is weighted further by a weight function, given as

$$\omega_\alpha=e^{-c\omega(t_\alpha-\tau)^2}, \quad (10)$$

where $\alpha = 1, 2, ..., n$.

Here, c, ω, and τ are called the tuning parameter, scale factor, and time-shift parameters, respectively. In this work, we chose the value of the tuning parameter as 0.005.

The WWZ power can be expressed in terms of weighted variations of the data set and is defined as

$$\mathrm{WWZ}=\frac{(N_{\rm eff}-3)V_y}{2(V_x-V_y)}, \quad (11)$$

where $N_{\rm eff}$ is the effective number density of data points and V_x and V_y are the weighted variations of data x and model function y, respectively. The distribution of the WWZ power in the colour-scaled diagram indicates the QPO in the data.

Both methods, i.e. LSP and WWZ, have their own challenges regarding gaps in the data or red noise. Therefore, by employing the combination of both these methods, they complement each other's advantages and disadvantages, ultimately increasing the reliability of our results when there is a common consensus from both methods, while ignoring cases with lower confidence.

To prepare the short-term LCs for periodicity analysis, we adopted the following approach (Agarwal et al. 2021). If we had a single data point in any passband (*BVRI*), then we used the corresponding observation directly. However, in the case of more than one measurement on a particular date in any passband, we estimated the weighted mean fluxes of that data set. The corresponding uncertainty associated with this mean flux value was taken as either the weighted standard deviation or the standard uncertainty of the weighted mean, whichever is larger.

3.3 Significance estimation

The statistical characteristics of the blazar light curve reveal a red-noise process (power-law type), even if the power plots produced by the LSP and WWZ techniques show distinct peaks. In the low-frequency range, the light curve may exhibit periodic behaviour of a few cycles as a result of this noise (Press 1978; Vaughan 2005). The power-spectrum response method (Uttley, McHardy & Papadakis 2002), widely used to model the periodogram, was employed to quantify the significance of the periodicity detection (Edelson et al. 2014; Bhatta et al. 2016a).

A power-law model was initially used to model the observed periodogram:

$$P(\nu)\propto\nu^{-\beta}+C, \quad (12)$$

where β and C represent the spectral index of the model and the Poissonian noise level, respectively, which is given by (Bhatta

---

[3] https://pyastronomy.readthedocs.io/en/latest/pyTimingDoc/pyPeriodDoc/gls.html

2019)

$$C = \frac{2T \langle F_{\rm err}^2 \rangle}{N^2 \mu^2}, \tag{13}$$

where N is the number of data points during the time span of observation T. The average flux and mean square of the flux errors are denoted by μ and $\langle F_{\rm err}^2 \rangle$, respectively. Our goal is to determine the power spectral density (PSD) model's best-fitting spectral index (β). We use the Timmer & Koenig (1995) technique to simulate 1000 light curves to determine this. Next, we compute the following χ^2-like values using the observed and re-sampled simulated periodograms:

$$\chi^2_{\rm obs} = \sum_{\nu=\nu_{\rm min}}^{\nu_{\rm max}} \frac{[\langle P_{\rm sim}(\nu) \rangle - P_{\rm obs}(\nu)]^2}{\langle \Delta P(\nu)_{\rm sim} \rangle^2}, \tag{14}$$

$$\chi^2_{{\rm sim},i} = \sum_{\nu=\nu_{\rm min}}^{\nu_{\rm max}} \frac{[\langle P_{\rm sim}(\nu) \rangle - P_i(\nu)]^2}{\langle \Delta P(\nu)_{\rm sim} \rangle^2}, \qquad i = 1, 2, ..., 1000. \tag{15}$$

Here, the minimum ($1/T$) and maximum ($N/(2T)$) temporal frequencies of the periodograms are denoted by $\nu_{\rm min}$ and $\nu_{\rm max}$. The simulated periodograms at a particular frequency are represented by the mean and standard deviation, $\langle P_{\rm sim}(\nu) \rangle$ and $\langle \Delta P(\nu)_{\rm sim} \rangle$.

Since the periodogram's powers are not Gaussian variables, the numbers above (equations 14 and 15) differ from the standard χ^2 distribution (Uttley et al. 2002). We have calculated the success fraction for every spectral index (β) to measure the fit quality. The ratio of the total number of χ_i^2 values for a specific spectral index to the number of $\chi^2_{{\rm sim},i}/\chi^2_{\rm obs} > 1$ values defines this. The best fit to the observed periodogram is provided by the β value at which the success fraction is highest. We fitted the success percentage versus β data using a Gaussian function to get the best-fitting spectral index. Equation (12) was used to describe the source periodogram. We then simulated 10 000 light curves for the best-fitting value of β, corresponding to the Gaussian function's peak and following the process described in Timmer & Koenig (1995). Using these simulated LCs, significance is estimated for ZDCF, LSP, and WWZ, as explained below.

ZDCF analysis: we estimated the correlation coefficients between the simulated LCs following the same process as we did for the observed data. In the next step we estimated the significance levels of the correlation coefficients of the observed data sets using the distribution of the simulated correlation coefficients corresponding to each time lag. One should keep in mind that the estimated significance assumes random flux variations in various energy bands, which is contradictory to what we have known through various past studies. Therefore, the significance is generally overestimated.

WWZ or LSP: the significance levels of any peak obtained through LSP and WWZ, which could be a possible QPO, are calculated by following a process similar to the above. Each simulated LC is used to calculate the LSP and WWZ power. Following this, we calculate the 90 per cent, 95 per cent, 99 per cent, 99.73 per cent, and 99.99 per cent confidence power and accordingly draw the contour lines for the respective significance levels for each LC in the LSP and WWZ power maps.

4 RESULTS

We observed the blazar BL Lacertae for a span of 16 nights in B, V, R, and I bands from 2020 September–October using six different optical telescopes. During the entire observation programme, about 5800 source frames were captured. The log of the observation campaign is given in Table 1, and the calibrated B, V, R, and I light curves are given in Fig. 1, where blue, green, red, and black colours represent the B, V, R, and I filters, respectively. The observation date, telescope used, and filters used are mentioned in each plot, along with the offsets used for clarity purposes when we have light curves in more than one band on a particular date.

4.1 Flux variability

To search for the presence of variability on intraday time-scales, we performed the statistical tests discussed in Sections 3.1.1 and 3.1.2. To ensure that we have sufficient data points to characterize IDV on a particular night, we selected only those light curves with an observation duration of more than 1 hour or with at least 10 data points for a single telescope. Following these criteria, we have 53 IDV LCs. The light curve is marked as variable (V) if the variability conditions of each test are satisfied at 3σ significance level. If conditions are satisfied for any two tests, then we denote the LC as probably variable (PV), otherwise the LC is marked non-variable (NV). Table 2 presents the results of variability analysis on intraday scales. We calculated the amplitude of variability on intraday time-scales of variables and possibly variable LCs using the equation described in Section 3.1.3, and the resultant amplitude values are given in column 8. For non-variable cases, we have put '...' in column 8.

As can be seen from Table 2, genuine IDV is detected in 39 out of 53 LCs, while three are possibly variable (LCs span a time-scale of 2–4 hours). The remaining 11 are non-variable. Although we have multiband observations for 2020 September 30 and October 4 (RRRT and KRK), we have variability only in the R band on 2020 September 30 and October 4 (KRK), while V, R displayed variability for 2020 October 4 (RRRT). The reason could be the somewhat shorter length of observations in the remaining filters.

The maximum IDV amplitude of $\sim$ 43 per cent was found on 2020 September 21 in the R-band LC observed with telescope C. Also, a greater amplitude of IDV is observed in higher energy bands (Table 2), as has been observed during several nights and also been found by previous studies on BL Lacertae (Nesci et al. 1998; Agarwal et al. 2023). Higher IDV amplitudes at shorter wavelengths indicate that the source spectrum gets flatter as the source brightness increases, while it gets steeper with decreasing brightness of the source (Prince et al. 2021). However, as can be seen from Table 2, in a few instances we found the trend was not followed, and the variability amplitude (A) was found to be larger at lower frequencies, which has also been found in the past (Gaur et al. 2019).

Fig. 2 illustrates the short-term LCs of BL Lacertae in B, V, R, and I passbands covering the entire observation duration. During 2020 September–October, the source reached the faintest state with R-band magnitude of 12.75 on 2020 September 23, while the brightest state was attained on 2020 October 5 with an R magnitude of 11.816. The brightest state attained by during our observation cycle is just 0.545 magnitudes fainter than the brightest state reached by BL Lacertae to date, i.e. $R = 11.271$ on 245 9426.493 (2021 July 30: Kunkel et al. 2021). LCs in all wavelengths display a genuine variability with flux variability amplitudes of 85.6 per cent, 78.9 per cent, 93.4 per cent, and 67.6 per cent in the B, V, R, and I passbands, respectively.

4.2 Colour variability

The quasi-simultaneous data in B, V, R, and I passbands acquired during our monitoring campaign on intraday and short time-scales allowed us to investigate the colour behaviour of the source BL Lacertae with its brightness in the R band. Such spectral variations

Table 2. Results from analysis of the intranight variability. The first column represents the observation date and the telescope used. The filter used and the number of observations (N) are listed in the second and third columns, respectively. The test results for C, F, and χ^2 tests are in the fourth, fifth, and sixth columns, respectively. The variability status is given in column 7, and the variability amplitude is given in column 8.

Date (Telescope) (yyyy mm dd)	Band	N	C test C	F test F, $F_c(0.99)$, $F_c(0.999)$	χ^2 test $\chi^2_{\rm av}$, $\chi^2_{0.99}$, $\chi^2_{0.999}$	Status	A %
2020.09.15 (A)	B	17	2.90	8.48, 3.34, 5.14	296.81, 32, 39.25	V	18.56
	V	192	4.17	17.42, 1.40, 1.57	5761.55, 239.38, 257.13	V	19.17
	R	16	2.92	8.54, 3.49, 5.46	187.01, 30.58, 37.7	V	7.53
	I	192	5.17	26.70, 1.40, 1.57	8465.65, 239.38, 257.13	V	17.28
2020.09.15 (C)	B	14	2.56	8.19, 3.86, 6.31	210.25, 27.69, 34.53	V	11.84
	V	15	3.13	9.82, 3.66, 5.85	234.64, 29.14, 36.12	V	10.53
	R	109	2.57	6.03, 1.57, 1.82	1.03×10^3, 145.1, 159.16	V	9.86
	I	13	3.17	10.06, 4.1, 6.9	193.72, 26.22, 32.91	V	8.55
2020.09.16 (B)	R	41	2.64	6.50, 2.11, 2.71	568.93, 63.7, 73.40	V	12.16
2020.09.17 (A)	B	12	5.33	28.62, 4.40, 7.62	1065, 24.72, 31.26	V	27.51
	V	199	2.95	8.68, 1.4, 1.55	2.91×10^3, 247.21, 265.23	V	24.25
	R	12	5.30	28.20, 4.4, 7.62	491.57, 24.72, 31.26	V	20.67
	I	176	2.60	5.68, 1.42, 1.6	2.33×10^3, 221.44, 238.55	V	15.95
2020.09.18 (C)	R	448	2.57	5.91, 1.25, 1.34	5.38×10^3, 519.5, 545.12	V	17.87
2020.09.19 (A)	V	54	1.07	1.16, 1.91, 2.37	129.20, 79.84, 90.57	NV	...
	R	58	1.04	1.11,1.86, 2.29	127.96, 84.73, 95.75	NV	...
2020.09.19 (B)	R	38	1.27	1.68, 2.17, 2.83	119.41, 59.8, 69.34	NV	...
2020.09.20 (A)	V	131	2.58	5.86, 1.51, 1.72	1.17×10^3, 170.42, 185.57	V	14.45
	R	128	2.68	7.22, 1.51, 1.74	1.40×10^3, 166.98, 182	V	14.06
2020.09.20 (B)	B	18	4.44	19.76, 3.21, 4.87	522.23, 33.41, 40.8	V	13.29
2020.09.21 (C)	B	16	9.19	84.39, 3.49, 5.46	2086.4, 30.58, 37.7	V	36.95
	V	16	13.50	182.15, 3.49, 5.46	4.39×10^3, 30.58, 37.7	V	34.78
	R	815	10.54	110.99, 1.17, 1.24	1.52×10^5, 910.8, 944.41	V	42.59
2020.09.22 (B)	R	40	2.94	8.67, 2.13, 2.75	792.52, 62.43, 72.05	V	14.95
2020.09.22 (C)	B	184	2.70	7.30, 1.41, 1.58	2.45×10^3, 230.42, 247.86	V	20.49
	V	189	3.14	9.88, 1.41, 1.57	3015.8, 236, 253.66	V	23.76
	R	184	3.50	12.28, 1.41, 1.58	3.95×10^3, 230.42, 247.86	V	18.86
	I	187	3.06	9.44, 1.41, 1.58	3.31×10^3, 233.8, 251.34	V	19.87
2020.09.27 (A)	B	39	3.30	10.91, 2.15, 2.79	740.73, 61.16, 70.7	V	17.35
	V	39	2.81	7.87, 2.15, 2.79	521.11, 61.16, 70.7	V	18.04
	R	310	4.70	22.12, 1.30, 1.42	1.25×10^4, 370, 391.55	V	19.87
	I	40	2.78	7.77, 2.13, 2.75	661.86, 62.43, 72.05	V	17.76
2020.09.30 (B)	B	18	1.68	2.87, 3.21, 4.87	81.66, 33.41, 40.8	NV	...
	V	18	2.22	4.94, 3.21, 4.87	155.96, 33.41, 40.8	PV	19.00
	R	18	3.94	15.51, 3.21, 4.87	392.82, 33.41, 40.8	V	14.54
2020.10.04 (B)	B	12	1.34	1.82, 4.4, 7.62	53.95, 24.72, 31.26	NV	...
	V	13	2.73	7.49, 4.1, 6.9	172.51, 26.22, 32.91	V	8.68
	R	14	2.84	8.05, 3.86, 6.31	218.09, 27.69, 34.53	V	8.93
2020.10.04 (C)	B	10	0.96	0.94, 5.26, 9.89	12.63, 21.67, 27.88	NV	...
	V	10	1.19	1.45, 5.26, 9.89	19.38, 21.67, 27.88	NV	...
	R	649	2.93	8.61, 1.20, 1.28	$1.24\ \times10^4$, 734.68, 764.97	V	21.55
	I	10	1.00	1.01, 5.26, 9.89	15.51, 21.67, 27.88	NV	...
2020.10.04 (E)	R	42	1.05	1.10, 2.08, 2.68	78.07, 64.95, 74.74	NV	...
2020.10.05 (A)	R	36	0.99	1.02, 2.22, 2.92	79.98, 57.34, 66.62	NV	...
2020.10.05 (C)	V	10	0.75	0.59, 5.26, 9.89	8.44, 21.67, 27.88	NV	...
	R	199	1.76	3.09, 1.4, 1.55	1.18×10^3, 247.21, 265.23	PV	11.44
2020.10.05 (E)	R	70	2.97	8.83, 1.75, 2.12	2.17×10^3, 99.23, 111.06	V	19.16
2020.10.06 (A)	B	74	1.79	3.25, 1.73, 2.08	406.36, 104.01, 116.1	PV	13.53
2020.10.06 (B)	B	15	2.75	7.56, 3.66, 5.85	221.06, 29.14, 36.12	V	19.00
	V	16	3.93	15.44, 3.49, 5.46	457.58, 30.58, 37.7	V	17.46
	R	16	3.70	13.72, 3.49, 5.46	576.73, 30.58, 37.7	V	15.27
2020.10.06 (C)	R	391	3.59	12.91, 1.27, 1.37	9.04×10^3, 457.9, 482.03	V	21.16
2020.10.06 (E)	R	105	3.84	14.77, 1.6, 1.84	5.47×10^3, 140.46, 154.31	V	17.69

help us understand the dominant variability mechanism in blazars better. The CMDs for our data sets on intraday time-scales are generated following the procedure detailed in Section 3.1.5. The resultant CMD plots on an intraday basis are presented in Fig. 3. The results of the linear correlation model are presented in Table 3. As evident from Table 3, the source dominantly displays a BWB trend on three nights, while the RWB trend occurs on only one night. The remainder of the nine nights show no significant trend on intraday time-scales, possibly due to too few data points on those nights.

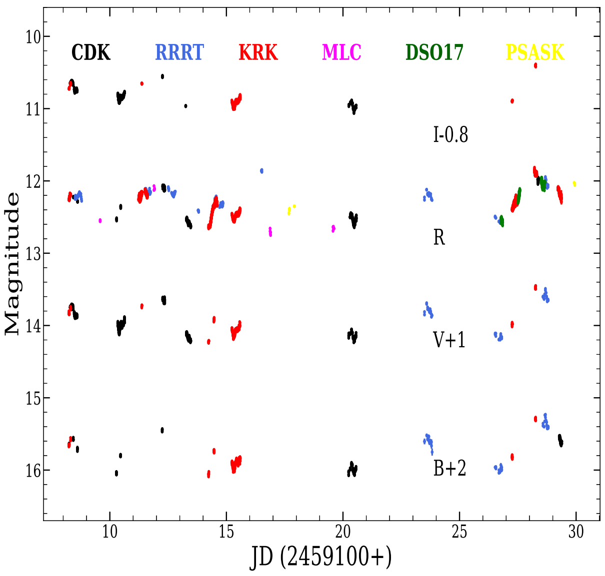

Figure 2. Short-term light curves of BL Lacertae in B, V, R, and I bands.

We also searched for the colour–magnitude relationship of the blazar on short time-scales. The CMD plots for the same are presented in Fig. 4, and the linear regression results are listed in Table 4. As can be seen from the results, the source displays a strong (r value ≥ 0.5 except for $V-R$) spectral hardening with increasing brightness (BWB trend). In the case of $V-R$, we get a positive correlation with p-value ≤ 0.01 but with r value ~ 0.4, indicating a weak correlation. Most of the CMDs in our study show significant BWB trends on intranight time-scales as well as on short time-scales, also observed by other authors (e.g. Papadakis et al. 2003, 2007; Stalin et al. 2006; Bhatta & Webb 2018). Both colour trends have been frequently observed in blazars (Stalin et al. 2006; Meng et al. 2017; Agarwal et al. 2021). BL Lacertae predominantly displays a BWB chromatism (Papadakis et al. 2007; Ikejiri et al. 2011; Agarwal et al. 2015; Gaur et al. 2015; Wierzcholska et al. 2015). Many studies have found a dependence of the BWB trend on the observed time-scale. Villata et al. (2002) reported strong BWB chromatic intranight time-scales but a mildly chromatic trend on longer time-scales (see also Villata et al. 2004a; Bhatta & Webb 2018; Gaur et al. 2019). Villata et al. (2004a) proposed that two components were present in the flux variability of BL Lacertae: a mildly chromatic component on a short time-scale, with a strong BWB one on an intraday time-scale. This was also confirmed by Ikejiri et al. (2011). They found that the rising part was bluer than the decaying part around the peak of the flare.

4.3 Time-lag analysis

We test the possibility of the existence of a time lag between *BVRI* bands on intraday or short time-scales using the DCF and ZDCF methods described in Section 3.1.6. Also, we determine the 99.99th, 99.73th, 99th, and 90th percentile levels of the distribution of cross-correlation values for each time-delay step by cross-correlating the simulated light curves using the approach described in Section 3.3. As the sampling distribution of DCF is skewed, the calculation of DCF uncertainties by the sample variances cannot be considered reliable. The ZDCFs adhere to a normal distribution with established mean and standard deviation, thus improving the reliability of uncertainty estimation for ZDCFs (Alexander 2013). Delays with a value smaller than the time gap between two consecutive frames of a particular band are not considered reliable. The results for our time-delay analysis on intraday and short time-scales are shown in Figs 5 and 6, respectively. The results of the ZDCF analysis on intraday to short time-scales are given in Tables 5 and 6, respectively. Both methods gave similar results but, due to the above reasons, we have shown results from the ZDCF methodology. Our results show a strong correlation (mostly with significance level of 99.99 per cent) between optical frequencies on intraday to short time-scales with no significant time delays, thus indicating the co-spatial nature of optical emission. Such multiband time-delay analysis helps in understanding the dominant emission mechanism within the emission region. Since the optical *BVRI* bands are very closely spaced, detecting time lags among them is difficult. As can be seen from Fig. 5, the ZDCF of 2020 September 19 is not significant, which could be because of poor sampling of the light curve. Maximizing the number of observations during a night in a band with better exposure values will be instrumental in the detection of time lag among the optical bands for future studies.

4.4 Periodicity

We binned our data following the approach described in Agarwal et al. (2021) to search for periodicity in our light curves, thereby removing the influence of different numbers of observation points per night on our periodicity analysis. Based on two distinct fundamental governing concepts, we utilized two of the most widely used time series methodologies: LSP and WWZ. A detailed description of both methods and significance estimation is given in Section 3.3. On each of the light curves, we used the 'PSRESP' significance estimate technique.

The results of our periodicity search in binned LCs of BL Lacertae covering the entire observation duration are given in Fig. 7. The upper left panel of Fig. 7 shows the LSP and WWZ results for BL Lacertae in the B passband, followed by V-band results in the upper right panel. The lower left and lower right panels display the LSP and WWZ periodicity results of the source in the R and I bands, respectively.

The B band has a total time span of 22 days (JD 245 9108–245 9129). The maximum power in the B-band LC is concentrated around the period of $\sim$ 5.3 days, which lasts throughout the observation period in the study. As can be seen from Fig. 7, there are other features, too, but none is significant with WWZ. The feature lying around $\sim$ 5.3 days in the B band is found to be above 3σ in local significance and has statistical significance following trial factor correction 2.21σ. We also searched for periodicity in other bands, i.e. V, R, and I. The V band displayed a possible period at 5.5 days with LSP at 3σ local significance and statistical significance 2.21σ after trial corrections during the 22-d observation period (JD 245 9108–245 9128). However, when the observation was decomposed into time and frequency domains using the WWZ technique, the same feature at $\sim$ 5.6 days period was detected but at relatively less significance (2.58σ). For the R-band LC during its 23-d observations (JD 245 9108–245 9129), LSP found peaks around $\sim$ 5.7 and 4.2 d with at least 3σ local significance and, with trial modifications, statistical significance 2.21σ, whereas with WWZ only the peak around $\sim$5.7 d is found to be significant; however, with less power. In the case of the I band, the total observation period is 21 days from JD 245 9108–245 9128. During this period, LSP analysis over the I-band LC display peaks at $\sim$ 5.5, 4.0, and 3.2 d with over 3σ local significance as well as 2.21σ statistical significance following trial modifications. In the WWZ result, the peak around $\sim$5.5 d is found to be the only persistent period, but with a lower significance of 2σ. Tripathi et al. (2024) also detected a periodicity of $\sim$5 d

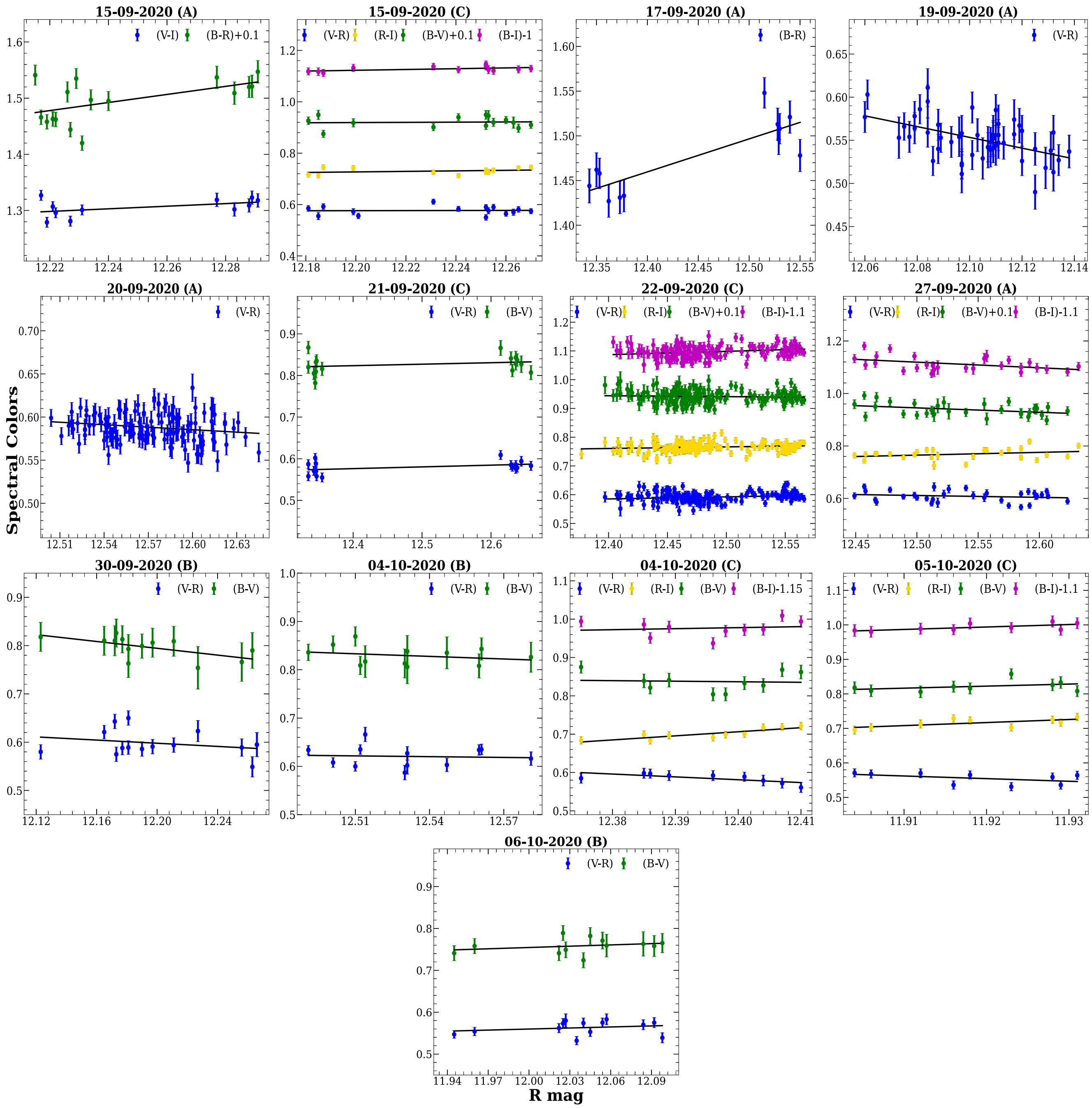

Figure 3. Colour indices versus R-band magnitude plots on an intraday time-scale. The least-squares fittings are overplotted with black lines. Observation dates are displayed at the top of each plot.

in *Transiting Exoplanet Survey Satellite* (*TESS*) light curves of BL Lacertae observed from 2019 September 12 for a total of 27 days.

4.5 Spectral energy distribution

From our observation period, we selected nights with quasi-simultaneous points in all four bands, i.e. *BVRI*, and obtained eight such nights. For these nights, we built the SEDs as described below. If a band had a single data point on a particular night, we used the corresponding flux value directly. However, we calculated the weighted mean flux for each band when multiple measurements were available during a given night. The averaging was performed over the same time interval (which was taken as the duration of the shortest LC on that particular night) for each band to avoid the influence of different durations of intraday light curves on the mean value. The error corresponding to the weighted mean flux was selected as the larger one between the weighted standard deviation and the standard uncertainty of the weighted mean. Fig. 8 shows the SEDs for each night in the $\log(F_\nu)$ versus $\log(\nu)$ representation. The effective frequencies for optical bands *BVRI* from Bessell, Castelli & Plez (1998) were used. The optical emission from blazars typically exhibits a simple power-law profile of the form $F_\nu = A\nu^\alpha$,

Table 3. Results of colour–magnitude analysis on intraday time-scales.

DATE	Colour	m	c	r	p
2020-09-15 (A)	$B-R$	0.72 ± 0.07	-7.40 ± 3.46	0.548	0.027
	$V-I$	0.23 ± 0.04	-1.54 ± 1.63	0.483	0.132
2020-09-15 (C)	$R-I$	0.10 ± 0.03	-0.53 ± 1.27	0.287	0.366
	$B-I$	0.15 ± 0.02	0.24 ± 0.94	0.520	0.083
	$V-R$	0.01 ± 0.04	0.39 ± 1.63	0.030	0.914
	$B-V$	0.04 ± 0.05	0.35 ± 2.23	0.058	0.843
2020-09-17 (A)	$B-R$	0.37 ± 0.022	-3.12 ± 0.92	0.832	<0.001
	$V-I$	-0.22 ± 0.23	4.09 ± 6.30	−0.193	0.714
2020-09-19 (A)	$V-R$	-0.62 ± 0.02	8.11 ± 1.86	−0.494	<0.001
2020-09-20 (A)	$V-R$	-0.10 ± 0.01	1.79 ± 0.56	−0.186	0.036
2020-09-21 (C)	$B-V$	0.03 ± 0.01	0.38 ± 0.46	0.241	0.368
	$V-R$	0.04 ± 0.01	0.06 ± 0.30	0.411	0.114
2020-09-22 (C)	$R-I$	0.06 ± 0.00	0.07 ± 0.34	0.153	0.045
	$B-I$	0.12 ± 0.00	0.74 ± 0.46	0.236	0.002
	$V-R$	0.07 ± 0.01	-0.30 ± 0.37	0.181	0.018
	$B-V$	-0.03 ± 0.01	1.23 ± 0.49	−0.060	0.437
2020-09-27 (A)	$R-I$	0.10 ± 0.01	-0.55 ± 0.86	0.288	0.145
	$B-I$	-0.21 ± 0.01	4.90 ± 1.08	−0.439	0.021
	$V-R$	-0.07 ± 0.01	1.50 ± 0.83	−0.180	0.317
	$B-V$	-0.17 ± 0.01	2.93 ± 0.90	−0.385	0.029
2020-09-30 (B)	$V-R$	-0.16 ± 0.05	2.60 ± 2.15	−0.250	0.389
	$B-V$	-0.35 ± 0.04	5.09 ± 1.68	−0.594	0.032
2020-10-04 (B)	$V-R$	-0.05 ± 0.07	1.28 ± 3.04	−0.066	0.839
	$B-V$	-0.18 ± 0.06	3.08 ± 2.66	−0.247	0.439
2020-10-04 (C)	$R-I$	1.06 ± 0.07	-12.49 ± 2.65	0.856	0.001
	$B-I$	0.26 ± 0.21	-1.16 ± 7.82	0.139	0.702
	$V-R$	-0.74 ± 0.09	9.78 ± 3.23	−0.709	0.032
	$B-V$	-0.14 ± 0.25	2.61 ± 9.25	−0.064	0.861
2020-10-05 (C)	$R-I$	0.88 ± 0.12	-9.82 ± 4.12	0.671	0.048
	$B-I$	0.71 ± 0.10	-6.40 ± 3.40	0.662	0.05
	$V-R$	-0.77 ± 0.18	9.68 ± 6.13	−0.466	0.206
	$B-V$	0.59 ± 0.19	-6.26 ± 6.40	0.364	0.335
2020-10-06 (B)	$V-R$	0.08 ± 0.03	-0.43 ± 1.22	0.229	0.452
	$B-V$	0.10 ± 0.03	-0.48 ± 1.34	0.269	0.398

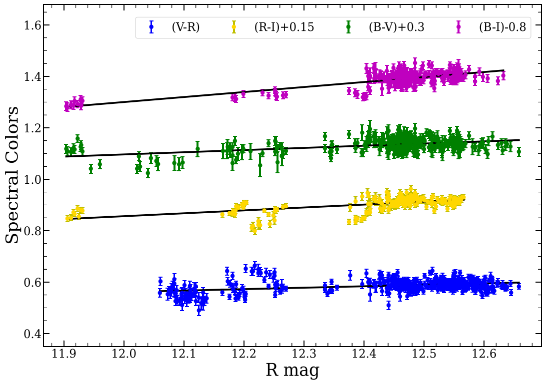

Figure 4. Colour indices versus R-band magnitude plot on a short time-scale, covering the entire monitoring duration.

where α is the optical spectral index. Therefore, to extract the optical spectral index, we used a linear polynomial of the form $\log(F_\nu) = -\alpha \log(\nu) + \mathrm{const}$ for the SED of each night. The results for the fit are summarized in Table 7. The optical spectral slopes for the source were found to be very steep, ranging from 2.90–3.16, thus indicating a negligible accretion disc contribution but strong synchrotron emission from the relativistic blazar jet (Wierzcholska et al. 2015; Zhang et al. 2023). During the entire monitoring period, the mean value of the spectral index was found to be 3.00. To study the evolution of spectral indices during the total observation period, we plotted spectral indices with JD and found that α did not vary significantly, as can be seen in Fig. 9.

Table 4. Results of the colour–magnitude analysis on a short-term basis.

Colour–magnitude	Slope	Intercept	r-value	p-value
$(B-I)$ versus R mag	0.194 ± 0.001	-0.234 ± 0.138	0.761	<0.001
$(B-V)$ versus R mag	0.085 ± 0.001	-0.220 ± 0.115	0.476	<0.001
$(R-I)$ versus R mag	0.113 ± 0.001	-0.649 ± 0.129	0.587	<0.001
$(V-R)$ versus R mag	0.056 ± 0.0002	-0.112 ± 0.084	0.374	<0.001

5 SUMMARY AND DISCUSSION

The flux variability of blazars over diverse time-scales ranging from a few minutes to decades is their characteristic feature (Raiteri et al. 2003; Villata et al. 2009; Hayashida et al. 2015; Gupta et al. 2016; Gaur et al. 2019; Agarwal et al. 2022; Priya et al. 2022) and provides useful insights about the emission region. Although several studies by various blazar monitoring groups have focused on variability analysis on time-scales of a few minutes at different wavelengths,

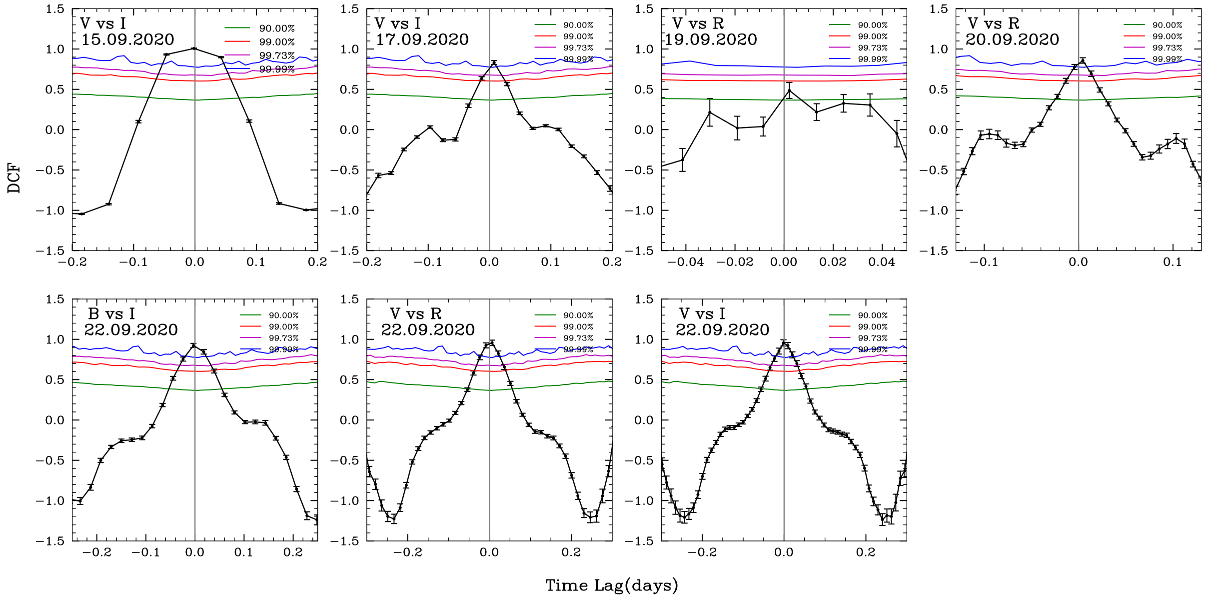

Figure 5. ZDCF plots between different frequency bands on an intraday basis. The observation date is mentioned in the upper left corner of each plot. The coloured lines indicate different significance levels as mentioned in the upper right panels of the plots.

Table 5. DCF results on intraday time-scales. The table displays the highest correlation coefficients in column 3 and the corresponding time lags in column 4 for the frequency bands given in column 2. Column 5 displays the significance level estimated for the corresponding wavelength pair of a particular date.

Date	Frequency bands	Correlation coefficients	Time lag (days)	Significance
2020-09-15	*V* versus *I*	$0.96^{+0.01}_{-0.01}$	$0.00^{+0.00}_{-0.00}$	99.99%
2020-09-17	*V* versus *I*	$0.86^{+0.02}_{-0.02}$	$0.00^{+0.00}_{-0.00}$	99.99%
2020-09-19	*V* versus *R*	$0.46^{+0.20}_{-0.23}$	$0.03^{+0.00}_{-0.00}$	90.00%
2020-09-20	*V* versus *R*	$0.83^{+0.03}_{-0.03}$	$0.00^{+0.00}_{-0.00}$	99.99%
2020-09-22	*B* versus *I*	$0.89^{+0.05}_{-0.06}$	$0.00^{+0.00}_{-0.00}$	99.99%
2020-09-22	*V* versus *R*	$0.96^{+0.01}_{-0.02}$	$0.00^{+0.00}_{-0.00}$	99.99%
2020-09-22	*V* versus *I*	$0.93^{+0.02}_{-0.03}$	$0.00^{+0.00}_{-0.00}$	99.99%

Table 6. DCF results on a short time-scale. As in Table 5, this table lists the highest correlation coefficients in column 2 and the corresponding time lags in column 3 for the frequency bands given in column 1. Column 4 displays the significance level estimated for the corresponding wavelength pair.

Frequency bands	Correlation coefficient	Time lag (days)	Significance
V versus *R*	$0.98^{+0.00}_{-0.01}$	$-0.17^{+0.00}_{-0.04}$	95%
B versus *R*	$0.99^{+0.00}_{-0.00}$	$0.16^{+0.03}_{-0.02}$	95%
B versus *I*	$0.99^{+0.00}_{-0.00}$	$0.16^{+0.40}_{-0.39}$	99%

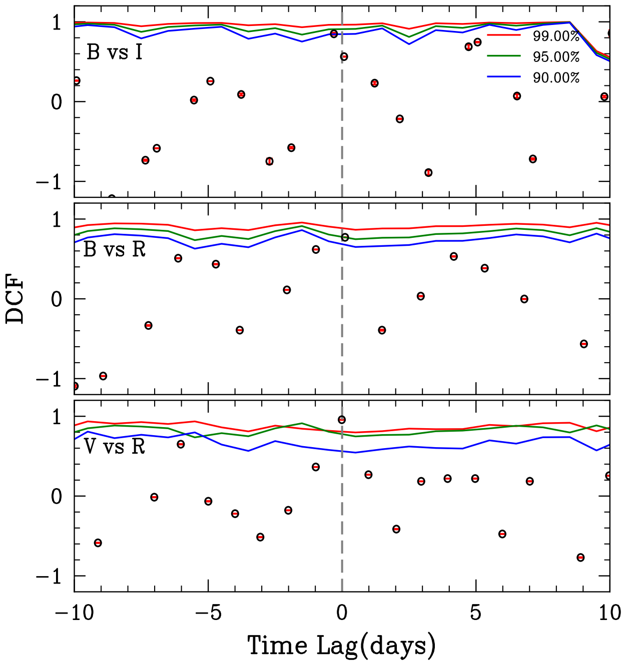

Figure 6. ZDCF results for the entire monitoring period. The coloured lines indicate different significance levels as mentioned in the upper right panel of the plots.

it is still one of the most puzzling issues of blazar physics and is still a matter of debate. The historical maxima of the source BL Lacertae provide us with an opportunity to understand the optical behaviour of the target better. In this work, we carried out a detailed temporal and spectral study of the blazar BL Lacertae during its recent activity in summer 2021 in multiple optical bands (*BVRI*) from 2021 September–October. We used several optical telescopes around the globe to monitor our target during the above period. Among the 53 IDV LCs, the source was found to display genuine IDV on 39 occasions, while three were possibly variable. Meanwhile, the source showed short-term flux variations in all optical bands. The flux variations observed in blazars are thought to arise from intrinsic physical processes, extrinsic scenarios, or a complex interplay of both factors. The flux and spectral variability of blazars present an intriguing phenomenon, and thus comprehensive understanding of these quantities necessitates considering both intrinsic and extrinsic factors.

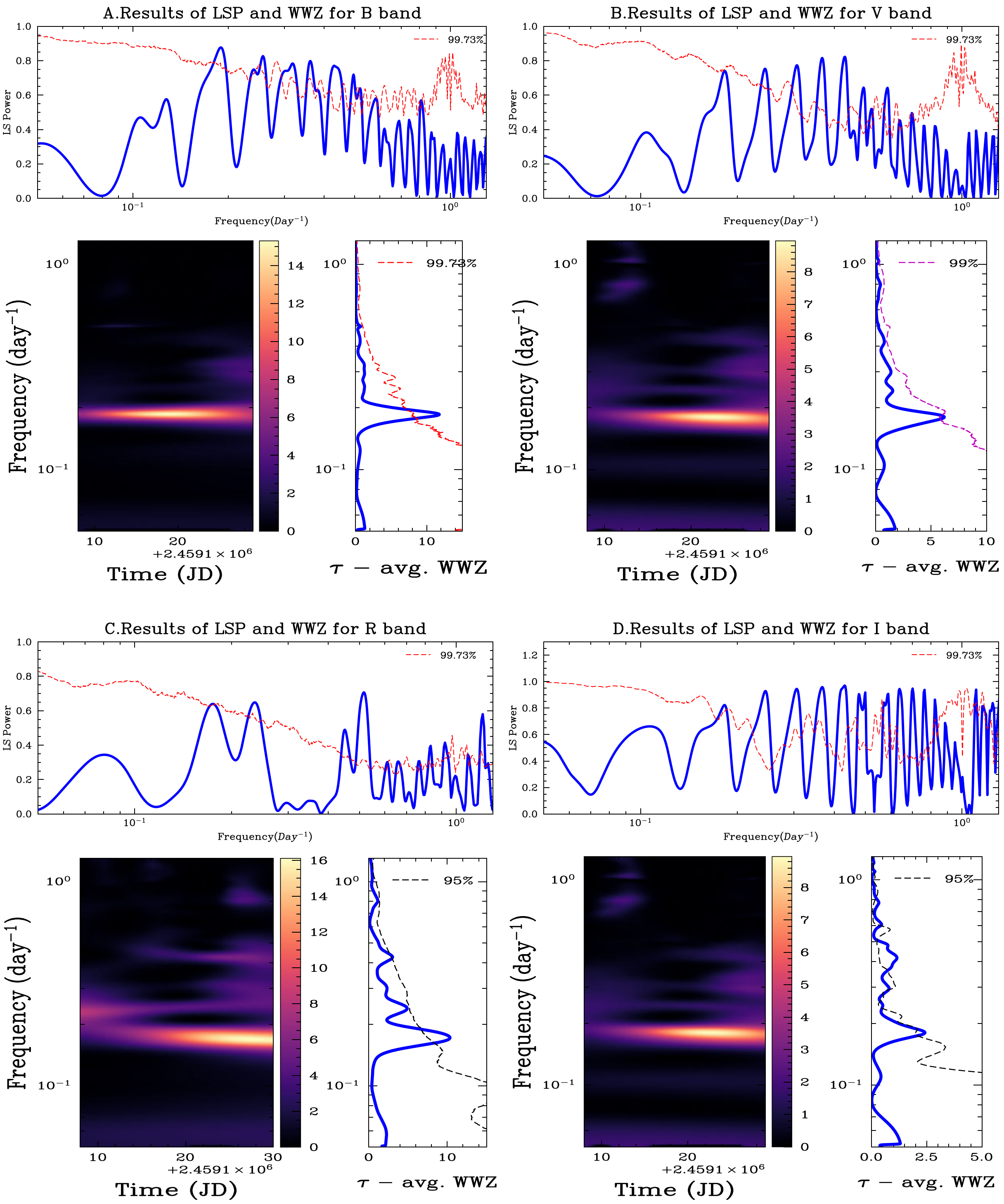
A.Results of LSP and WWZ for B band

B.Results of LSP and WWZ for V band

C.Results of LSP and WWZ for R band

D.Results of LSP and WWZ for I band

Figure 7. Lomb–Scargle periodogram and weighted wavelet Z-transform of nightly binned B (upper left panel), V (upper right panel), R (bottom left panel), and I (bottom right panel) LCs. The dashed curves represent the contours of corresponding local significance.

The intrinsic factors are associated with changes in the accretion rate or the shock propagating along the helical jet of blazars while interacting with the irregularities in the jet flow, particle injection, and energy loss, or variation in the direction or speed of the jet (Hughes, Aller & Aller 1992; Kirk, Rieger & Mastichiadis 1998; Larionov et al. 2013). The dominant emission model for intrinsic IDV in blazars is internal shocks propagating along their relativistic jets (Kirk et al. 1998). According to the homogenous single-zone leptonic emission model of blazars, the shock propagating along the cylindrical jet, interacting with irregularities along the flow, can lead to gradual particle acceleration (either electrons or positrons) at the shock front to energies equivalent to Lorentz factors of thousands (Marscher et al. 2008; Joshi & Böttcher 2011) and followed by radiative cooling in the emission region. The more energetic the

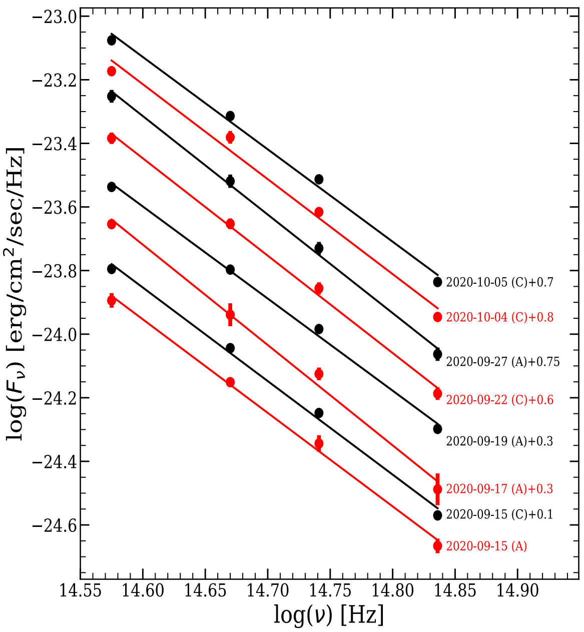

Figure 8. Spectral energy distributions of BL Lacertae in B, V, R, and I bands. The observation date and the offset used to shift the plots for clarity are mentioned in the plot.

Table 7. Straight-line fits to optical SEDs of the blazar.

Date	α	c	r	p
2020-09-15 (A)	2.941 ± 0.060	18.990 ± 1.532	−0.998	0.002
2020-09-15 (C)	2.962 ± 0.064	19.304 ± 1.633	−0.998	0.002
2020-09-17 (A)	3.156 ± 0.084	22.055 ± 2.128	−0.997	0.003
2020-09-19 (A)	2.896 ± 0.053	18.387 ± 1.343	−0.998	0.001
2020-09-22 (C)	3.062 ± 0.057	20.653 ± 1.453	−0.998	0.001
2020-09-27 (A)	3.098 ± 0.059	21.166 ± 1.494	−0.998	0.001
2020-10-04 (C)	2.986 ± 0.110	19.577 ± 2.809	−0.994	0.006
2020-10-05 (C)	2.904 ± 0.075	18.575 ± 1.901	−0.997	0.003

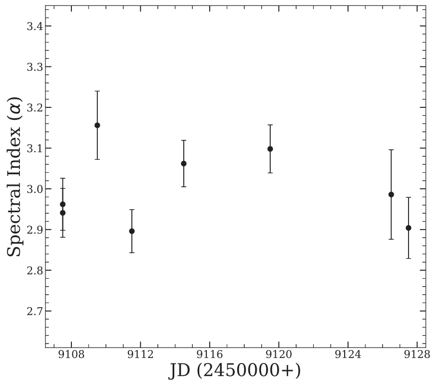

Figure 9. Variation of spectral indices calculated from SED analysis at different epochs.

particles, the quicker they lose energy, due to the fact that the energy losses due to synchrotron or inverse Compton scale with the particle energy, i.e. $\dot{\gamma} \propto -\gamma^2$. The interplay between acceleration and subsequent particle cooling leads to magnetohydrodynamical instability in the jet. Such magnetohydrodynamical instabilities can disrupt the magnetic field structure by twisting magnetic field lines, thus dictating the flare's rise and decay phases in a light curve. An alternative scenario for the detected variability then arises, which revolves around magnetic reconnection within a magnetically dominant jet (Chiuderi, Pietrini & Ciamponi 1989; Petropoulou, Giannios & Sironi 2016). The emission would originate from the turbulent plasma in the form of plasmoids or fast-moving magnetic filaments in the reconnection region. Similar to the jet-in-jet model, strong magnetic reconnection could generate mini-jets, thus releasing a substantial amount of magnetic energy, energizing the surrounding plasma, and consequently accelerating particles and thereby causing the observed fast variability.

Alternatively, extrinsic factors associated with the motion and geometry of the emitting region/blob can also contribute to the observed variable emission. A geometric origin of variability includes a change in the Doppler factor of the emission region due to variation in the viewing angle of the blob/emission region (Raiteri et al. 2017) when the jet undergoes dynamical orientations or rotation. This causes variations in the orientation of different emission regions and hence their relative Doppler factors (the Doppler factor, δ, of the emitting region, is defined as $1/\Gamma(1 - \beta \cos \theta_{\rm obs})$, where Γ is the bulk Lorentz factor, β is the speed of the emission region in units of the speed of light (c), and θ is the angle of the jet with respect to our line of sight). When the emission regions are oriented along the observer's line of sight, their emission is amplified due to relativistic Doppler boosting. These geometric variations can mimic the rise and fall of the light curves and can be perceived as a flare.

From Table 2, we note that the variability amplitude was highest (∼ 43 per cent) when the source was in a faint state, which is possible if the flux increase is due to a uniform flow of particles in the Doppler-boosted jet. In this scenario, the variability amplitude on an intranight basis due to turbulence inside the jet decreases in magnitude (Marscher 2014). The realistic optical variability could be shaped by both source intrinsic and extrinsic scenarios, along with the existence of multiple emitting regions.

The flux variations from blazars in the optical and infrared are accompanied by spectral variations. Colour–magnitude studies of blazars in the past have shown mixed trends, i.e. BWB (Stalin et al. 2009) or RWB (Bonning et al. 2012) or a combination of both (Agarwal et al. 2023) or no spectral variations (Raiteri et al. 2003; Poon et al. 2009). The observed spectral evolution in BL Lacs has normally been found to become bluer with an increase in brightness, i.e. a BWB trend (Vagnetti, Trevese & Nesci 2003; Bhatta & Webb 2018; Priya et al. 2022; Diwan et al. 2023, and references therein). The spectral evolution of BL Lacertae during our observation period displays a BWB chromatism on intraday to short-term time-scales, except in a few intranight light curves where we observed an opposite pattern, i.e. RWB chromatism (see Section 4). Such colour changes can be attributed to the contributions from the relativistic jet at optical frequencies. The BWB behaviour can be explained by an increase in variability amplitude at higher frequencies owing to the injection of accelerated electrons with a harder energy distribution compared with earlier cooler ones (Kirk et al. 1998; Mastichiadis & Kirk 2002).

Blazar flux variations have been found to be mostly aperiodic due to dominant red noise, but a small fraction of them have shown the presence of statistically significant periods in their multi-frequency LCs (Sandrinelli et al. 2016; Peñil et al. 2020; Jorstad et al. 2022; Tripathi et al. 2024), thus leading to a hunt for periodic signals over the last decades. Such periodic emission from blazars provides us with a wealth of information about the nature of the source and the processes occurring in the innermost violent regions, which are otherwise inaccessible to us. Several processes have been proposed to interpret the periodicity in blazars: for instance, the supermassive binary BH system proposed for two famous blazars, namely PG 1553 + 113, which is famous for its 2.18-year periodicity in its γ-ray LCs from the *Fermi* Large Area Telescope (LAT: Ackermann et al. 2015), and OJ 287, where ∼12-year periodicity has been detected in its optical light curves (Sillanpaa et al. 1988; Valtonen et al. 2011). Several other alternative explanations have been proposed to explain the apparent periodicity in blazars. Some of them are the lighthouse effect (Camenzind & Krockenberger 1992), internal helical structure of the jet and magnetic field (Rieger 2004; Raiteri et al. 2017), periodic shocks, shocks propagating outward along the jet, and periodic oscillations of the accretion flow (Piner, Pant & Edwards 2010; Mohan & Mangalam 2015). Some of the popular methods to interpret the period over a time-scale of a few days (similar to what we found here) could be based on the existence of oscillations in the inner region of the accretion disc, which are propagated further into the jet. Blazar emission, especially for BL Lac sources, is predominantly non-thermal and originates from the Doppler-boosted jet. As these jets are aligned along the observer's line of sight, the overall emission is amplified relativistically over the entire electromagnetic spectrum. Therefore, periodicity in the case of BL Lacertae can be inferred in the framework of the model based on kink instability internal to the jet, as discussed by Jorstad et al. (2022), who studied BL Lacertae in optical and γ-rays using observations collected between 2020 March and December. The authors reported a periodic feature at the 0.57-d period, which they explained by the kink instability model, where kind instabilities are a form of current-driven plasma instabilities.

According to magnetohydrodynamic simulations, the strong toroidal magnetic field in the jet and the resultant increase in particle acceleration, along with the twisting of toroidal field lines, can lead to the formation of a quasi-periodic kink. As the kink instability grows with time in the region of compressed plasma, we observe a QPO feature over a time-scale of a few days or even weeks to months. The period of QPOs ($T_{\rm obs}$) associated with the kink instability in the observer's frame is calculated as (Dong, Zhang & Giannios 2020)

$$T_{\rm obs} = \frac{R_{KI}}{\langle v_{\rm tr} \rangle \, \delta}, \tag{16}$$

where R_{KI} is the transverse displacement of the jet from its centre or the size of the emission region, $\langle v_{\rm tr} \rangle$ is the average velocity of motion, and δ is the Doppler factor. R_{KI} typically ranges from 10^{16}–10^{17} cm for a typical BL Lac object, while $\langle v_{\rm tr} \rangle$ has been derived as $\approx 0.16c$ by Dong et al. (2020). Using $\delta = 15$ for BL Lacertae as derived by Jorstad et al. (2001) using the Very Large Baseline Array, $T_{\rm obs}$ lies in the range 1–10 days, which is consistent with the QPO claimed in this work. Alternatively, other processes that can be used to explain the periodicity on time-scales of a few days for Seyferts or quasars where disc emission plays an important role include periodic oscillations of the accretion disc, turbulence in the accretion flow, or Lens–Thirring precession of the inner accretion disc. A number of issues, such as the impact of noise and periodic features lasting only for a few cycles, lead to fake detection; thus, periodicity detection in blazars continues to be a controversial research area.

To summarize, we conducted a study of optical photometric data for BL Lacertae obtained using six different ground-based optical telescopes around the globe from 2020 September–October and collected ∼5800 photometric image frames in *BVRI*. We examined 53 IDV LCs using three robust statistical analysis methods, namely, C, F, and χ^2 tests. Genuine IDV is detected in 39 LCs (42 if we include PV cases). The remaining 11 LCs did not show any genuine variability. As pointed out by Gupta & Joshi (2005), if the source is observed for less than 6 h, the chance of variability detection is 60–65 per cent. However, if the source is monitored for more than 6 h, the chance of detecting genuine variability increases to 85 per cent. The 11 LCs displaying no variability are gathered over a duration of 2–5 h; therefore, if we had observed the source for more than 6 h, the probability of the LC being variable would have increased. The target significant variability on shorter time-scales with variability amplitudes was 85.6 per cent, 78.9 per cent, 93.4 per cent, and 67.6 per cent in B, V, R, and I passbands, respectively. Analysing the colour–magnitude relationship of the source on both intraday and short time-scales, we found dominantly bluer-when-brighter behaviour. Correlation analysis using ZDCF indicates a strong correlation between *BVRI* and null time lags. Based on our periodicity search using LSP and WWZ, we found a QPO of ∼5.5 days in the *BVRI* passband with a local significance of 3σ and a global significance of $\geq 2.21\sigma$, which we explained using the kink instability model. Further, to determine the optical spectral indices, we generated SEDs at different epochs with quasi-simultaneous observations in all four bands and found the spectral index to range from 2.9–3.2, which can be attributed to a strong jet contribution. Further densely sampled observations with enhanced sensitivity, along with theoretical models, can aid in unravelling the full story behind such captivating blazar events.

DATA AVAILABILITY

The data of this article will be shared one year after the publication of this work on reasonable request to the first author.

REFERENCES

Abdo A. A. et al., 2010, ApJ, 722, 520

Ackermann M. et al., 2011, ApJ, 743, 171

Ackermann M. et al., 2015, ApJ, 813, L41

Agarwal A., 2023, ApJ, 946, 109

Agarwal A. et al., 2015, MNRAS, 451, 3882

Agarwal A. et al., 2021, A&A, 645, A137

Agarwal A., Pandey A., Özdönmez A., Ege E., Kumar Das A., Karakulak V., 2022, ApJ, 933, 42

Agarwal A. et al., 2023, ApJS, 265, 51

Alexander T., 1997, in Maoz D., Sternberg A., Leibowitz E. M., eds, Astrophysics and Space Science Library Vol. 218, Astronomical Time Series. p. 163

Alexander T., 2013, preprint (arXiv:1302.1508)

Ansoldi S. et al., 2018, ApJ, 863, L10

Begelman M. C., Sikora M., 1987, ApJ, 322, 650

Bessell M. S., Castelli F., Plez B., 1998, A&A, 333, 231

Bhatta G., 2019, MNRAS, 487, 3990

Bhatta G., 2021, ApJ, 923, 7

Bhatta G., Webb J., 2018, Galaxies, 6, 2

Bhatta G. et al., 2016a, ApJ, 831, 92

Bhatta G. et al., 2016b, ApJ, 832, 47

Blanch O., 2020a, The Astronomer's Telegram, 13963, 1

Blanch O., 2020b, The Astronomer's Telegram, 14032, 1

Bonning E. et al., 2012, ApJ, 756, 13

Böttcher M., Reimer A., Sweeney K., Prakash A., 2013, ApJ, 768, 54

Camenzind M., Krockenberger M., 1992, A&A, 255, 59

Cheung C. C., 2020, The Astronomer's Telegram, 13933, 1

Chiuderi C., Pietrini P., Ciamponi G. T., 1989, ApJ, 339, 70

Diwan R. et al., 2023, MNRAS, 524, 4333

Dong L., Zhang H., Giannios D., 2020, MNRAS, 494, 1817

Edelson R. A., Krolik J. H., 1988, ApJ, 333, 646

Edelson R., Vaughan S., Malkan M., Kelly B. C., Smith K. L., Boyd P. T., Mushotzky R., 2014, ApJ, 795, 2

Foffano L., Prandini E., Franceschini A., Paiano S., 2019, in 36th International Cosmic Ray Conference (ICRC2019), Vol. 36. p. 676
Fossati G., Celotti A., Ghisellini G., Maraschi L., 1997, MNRAS, 289, 136
Foster G., 1996, AJ, 112, 1709
Gaur H. et al., 2015, MNRAS, 452, 4263
Gaur H. et al., 2019, MNRAS, 484, 5633
Ghisellini G., 2019, Rendiconti Lincei. Scienze Fisiche e Naturali, 30, 137
Ghisellini G., Celotti A., 2001, A&A, 379, L1
Ghisellini G., Maraschi L., 1989, ApJ, 340, 181
Ghisellini G. et al., 1997, A&A, 327, 61
Gopal-Krishna, Stalin C. S., Sagar R., Wiita P. J., 2003, ApJ, 586, L25
Grishina T. S., Larionov V. M., 2020, The Astronomer's Telegram, 13930, 1
Gupta A. C., Joshi U. C., 2005, A&A, 440, 855
Gupta A. C. et al., 2016, MNRAS, 458, 1127
Hagen-Thorn V. A., Larionov V. M., Hagen-Thorn A. V., Jorstad S. G., Temnov G. O., 2002, in Green R. F., Khachikian E. Y., Sanders D. B., eds, ASP Conf. Ser. Vol. 284, IAU Colloq. 184: AGN Surveys. San Francisco. p. 363
Hayashida M. et al., 2015, ApJ, 807, 79
Heidt J., Wagner S. J., 1996, A&A, 305, 42
Hervet O., Boisson C., Sol H., 2016, A&A, 592, A22
Hughes P. A., Aller H. D., Aller M. F., 1992, ApJ, 396, 469
Ikejiri Y. et al., 2011, PASJ, 63, 639
Jankowsky F., Wagner S., 2020, The Astronomer's Telegram, 13956, 1
Jorstad S. G., Marscher A. P., Mattox J. R., Aller M. F., Aller H. D., Wehrle A. E., Bloom S. D., 2001, ApJ, 556, 738
Jorstad S. G. et al., 2022, Nature, 609, 265
Joshi M., Böttcher M., 2011, ApJ, 727, 21
Kirk J. G., Rieger F. M., Mastichiadis A., 1998, A&A, 333, 452
Kunkel L. et al., 2021, The Astronomer's Telegram, 14820, 1
Larionov V. M. et al., 2013, ApJ, 768, 40
Lomb N. R., 1976, Ap&SS, 39, 447
Maraschi L., Ghisellini G., Celotti A., 1992, ApJ, 397, L5
Marchini A. et al., 2021, The Astronomer's Telegram, 14328, 1
Marscher A. P., 2014, ApJ 780 87
Marscher A. P. et al., 2008, Nature, 452, 966
Mastichiadis A., Kirk J. G., 2002, PASA, 19, 138
Meng N., Wu J., Webb J. R., Zhang X., Dai Y., 2017, MNRAS, 469, 3588
Mohan P., Mangalam A., 2015, ApJ, 805, 91
Montagni F., Maselli A., Massaro E., Nesci R., Sclavi S., Maesano M., 2006, A&A, 451, 435
Nesci R., Maesano M., Massaro E., Montagni F., Tosti G., Fiorucci M., 1998, A&A, 332, L1
Neshpor Y. I., Chalenko N. N., Stepanian A. A., Kalekin O. R., Jogolev N. A., Fomin V. P., Shitov V. G., 2001, Astron. Rep., 45, 249
Nilsson K. et al., 2018, A&A, 620, A185
Ojha R., Valverd J., 2020, The Astronomer's Telegram, 13964, 1
Papadakis I. E., Boumis P., Samaritakis V., Papamastorakis J., 2003, A&A, 397, 565
Papadakis I. E., Villata M., Raiteri C. M., 2007, A&A, 470, 857
Peñil P. et al., 2020, ApJ, 896, 134
Petropoulou M., Giannios D., Sironi L., 2016, MNRAS, 462, 3325
Piner B. G., Pant N., Edwards P. G., 2010, ApJ, 723, 1150
Poon H., Fan J. H., Fu J. N., 2009, ApJS, 185, 511
Press W. H., 1978, Comments on Modern Physics, Part C – Comments on Astrophysics, 7, 103
Press W. H., Rybicki G. B., 1989, ApJ, 338, 277
Prince R., Agarwal A., Gupta N., Majumdar P., Czerny B., Cellone S. A., Andruchow I., 2021, A&A, 654, A38
Priya S., Prince R., Agarwal A., Bose D., Özdönmez A., Ege E., 2022, MNRAS, 513, 2239
Raiteri C. M. et al., 2003, A&A, 402, 151
Raiteri C. M. et al., 2009, A&A, 507, 769
Raiteri C. M. et al., 2013, MNRAS, 436, 1530
Raiteri C. M. et al., 2017, Nature, 552, 374
Rieger F. M., 2004, ApJ, 615, L5
Romero G. E., Cellone S. A., Combi J. A., 1999, A&AS, 135, 477
Sahakyan N., Giommi P., 2022, MNRAS, 513, 4645
Sandrinelli A., Covino S., Dotti M., Treves A., 2016, AJ, 151, 54
Sandrinelli A. et al., 2017, A&A, 600, A132
Sasada M., Imazawa R., Hazama N., Fukazawa Y., 2020, The Astronomer's Telegram, 14081, 1
Scargle J. D., 1982, ApJ, 263, 835
Sikora M., Begelman M. C., Rees M. J., 1994, ApJ, 421, 153
Sillanpaa A., Haarala S., Valtonen M. J., Sundelius B., Byrd G. G., 1988, ApJ, 325, 628
Stalin C. S., Gopal-Krishna, Sagar R., Wiita P. J., Mohan V., Pandey A. K., 2006, MNRAS, 366, 1337
Stalin C. S. et al., 2009, MNRAS, 399, 1357
Steineke R. et al., 2020, The Astronomer's Telegram, 13958, 1
Stetson P. B., 1987, PASP, 99, 191
Stetson P. B., 1992, in Worrall D. M., Biemesderfer C., Barnes J., eds, ASP Conf. Ser. Vol. 25, Astronomical Data Analysis Software and Systems I. p. 297
Timmer J., Koenig M., 1995, A&A, 300, 707
Tripathi A., Smith K. L., Wiita P. J., Wagoner R. V., 2024, MNRAS, 527, 9132
Urry C. M., Padovani P., 1995, PASP, 107, 803
Uttley P., McHardy I. M., Papadakis I. E., 2002, MNRAS, 332, 231
Vagnetti F., Trevese D., Nesci R., 2003, ApJ, 590, 123
Valtonen M. J., Lehto H. J., Takalo L. O., Sillanpää A., 2011, ApJ, 729, 33
Vaughan S., 2005, A&A, 431, 391
Vermeulen R. C., Ogle P. M., Tran H. D., Browne I. W. A., Cohen M. H., Readhead A. C. S., Taylor G. B., Goodrich R. W., 1995, ApJ, 452, L5
Villata M., Raiteri C. M., Lanteri L., Sobrito G., Cavallone M., 1998, A&AS, 130, 305
Villata M. et al., 2002, A&A, 390, 407
Villata M. et al., 2004a, A&A, 421, 103
Villata M. et al., 2004b, A&A, 424, 497
Villata M. et al., 2009, A&A, 501, 455
Wagner S. J., Witzel A., 1995, ARA&A, 33, 163
Weaver Z. R. et al., 2020, ApJ, 900, 137
Wierzcholska A., Ostrowski M., Stawarz Ł., Wagner S., Hauser M., 2015, A&A, 573, A69
Zhang B.-K., Tang W.-F., Wang C.-X., Wu Q., Jin M., Dai B.-Z., Zhu F.-R., 2023, MNRAS, 519, 5263
Zibecchi L., Andruchow I., Cellone S. A., Carpintero D. D., Romero G. E., Combi J. A., 2017, MNRAS, 467, 340
Zibecchi L., Andruchow I., Cellone S. A., Carpintero D. D., 2020, MNRAS, 498, 3013
Zola S., Kouprianov V., Reichart D. E., Bhatta G., Caton D. B., 2021, in Rev. Mex. Astron. Astrofis. Conf. Ser. Vol. 53. p. 206

This paper has been typeset from a TEX/LATEX file prepared by the author.